

Mechanical and electronic properties of α - M_2X_3 (M =Ga, In; X =S, Se) monolayersGuitao Zhang,¹ Kangjun Lu,¹ Yifan Wang,¹ Haowei Wang,² and Qian Chen^{1,*}¹*School of Physics, Southeast University, Nanjing 211189, China*²*Department of Mechanical Engineering, California State University Fullerton, Fullerton, California 92831, USA*

(Received 13 January 2022; revised 13 June 2022; accepted 14 June 2022; published 23 June 2022)

Due to the atomic level thickness and novel properties, two-dimensional (2D) materials have received extensive attention on the research and application of future nanodevices. In this paper, the mechanical and electronic properties of α - M_2X_3 ($M = \text{Ga, In}; X = \text{S, Se}$) monolayers are studied to explore their applications in 2D electronic devices. First-principles calculations based on density functional theory indicate that these four α - M_2X_3 monolayers are all semiconductors and possess Young's modulus of less than 100 N m^{-1} with a deformation range up to about 30%. In addition, the carrier mobility of the α - M_2X_3 monolayer exceeds $600 \text{ cm}^2 \text{ V}^{-1} \text{ s}^{-1}$ and remains high under strain. In particular, because the band edge shifts under compressive strain, the electron mobility of the α - Ga_2S_3 monolayer increases to about $1800 \text{ cm}^2 \text{ V}^{-1} \text{ s}^{-1}$ at -3% strain, which is approximately three times the value without strain. The excellent ductility and strain-promoted electronic properties make the 2D α - M_2X_3 promising candidates for the application of flexible electronic devices.

DOI: [10.1103/PhysRevB.105.235303](https://doi.org/10.1103/PhysRevB.105.235303)**I. INTRODUCTION**

Two-dimensional (2D) materials with only one or few atomic layers have attracted wide interest for their unique size advantage and novel physical properties, such as electronics [1,2], optics [3], magnetism [4,5], and mechanics [6,7]. The ultrathin thickness makes 2D materials a great candidate for flexible electronic devices and to realize the multifunctional electronic skin that integrates various kinds of transistors, gate circuits, sensors, and other components [8–13]. Compared to the organic molecular thin-film materials commonly used in flexible devices, inorganic 2D semiconductors have advantages not only in thickness, but also in electronic properties, such as mobility and exciton lifetime. However, the lack of ductility hinders the wide application of inorganic materials in this field. Many organic materials can bear stupendous deformation, even reaching or exceeding 100% [14], but most inorganic semiconductors can only withstand a very small deformation, generally about 10% (for example, 6%–11% for MoS_2 [15], 12% for hexagonal boron nitride (*h*-BN) [16] and 6% for CrI_3 [17]). Nevertheless, Chen *et al.* reported that α - Ag_2S with the layered structure exhibits an extraordinary ductility at a high plastic deformation strain [14], which opened up the possibility of finding malleable 2D inorganic semiconductors for flexible electronic devices.

Very recently, Ga_2S_3 nanosheets of large sizes were successfully synthesized by chemical vapor deposition (CVD) [18], and 2D III–VI group compounds have begun to attract people's attention. These 2D semiconductors have been found to have many excellent properties, such as high light sensitivity and fast response [19], intrinsic 2D ferroelectric properties [20], and considerable in-plane and out-of-plane piezoelec-

tricity [21]. It should be emphasized that these compounds are also low cost, nontoxic, and environmental friendly [22]. To explore the possible applications of 2D III–VI group materials in flexible electronic devices, the mechanical properties of α - M_2X_3 ($M = \text{Ga, In}; X = \text{S, Se}$) monolayer were studied by first-principles calculations in this paper. In addition, the effect of strain on electronic properties and the stability of these materials were investigated. Our paper shows that the four α - M_2X_3 monolayers have low Young's modulus and high ductility. They can withstand high plastic deformation up to 30%. The carrier mobility of the α - Ga_2S_3 monolayer exceeds $600 \text{ cm}^2 \text{ V}^{-1} \text{ s}^{-1}$ and can be further promoted under strain.

II. COMPUTATIONAL METHOD

All calculations were performed within the framework of density functional theory implemented in the Vienna *ab initio* simulation package [23]. The electron-electron interactions were treated by a general gradient approximation parametrized by Perdew-Burke-Ernzerhof (PBE) [24]. A kinetic-energy cutoff of 500 eV was set for the plane-wave expansion to ensure convergence [25]. A vacuum space of more than 20 \AA was introduced in the perpendicular plane to avoid the interlayer interactions. Electronic minimization was performed with a tolerance of 10^{-7} eV , and ionic relaxation was performed with a force tolerance of $10^{-3} \text{ eV \AA}^{-1}$ on each ion. A Γ -centered $11 \times 11 \times 1$ Monkhorst-Pack k -point mesh [26] was used for Brillion-zone sampling. A denser $21 \times 21 \times 1$ mesh was used for electronic structure calculation. Hyed-Scuseria-Ernzerhof (HSE06) [27,28] was used to obtain more accurate electronic band structures. The force constants were calculated using a $4 \times 4 \times 1$ supercell, and the data processing was performed by the PHONOPY code to find phonon frequencies [29].

*qc119@seu.edu.cn

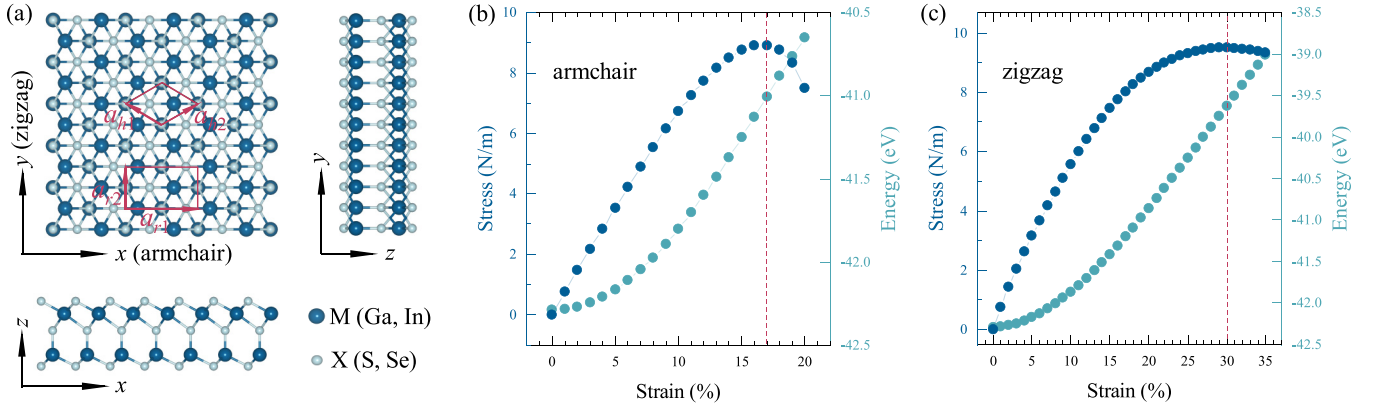


FIG. 1. (a) Atomic structure of α - M_2X_3 monolayers where the diamond box represents the unit cell, and the rectangular box represents the supercell used in this paper. The stress of the α - Ga_2S_3 monolayer under uniaxial stretching along (b) the armchair and (c) the zigzag directions where the vertical dashed line indicates the position of maximum stress.

For 2D materials, the stress was calculated using the Hellmann-Feynman theorem [30], which is modified to be the force on unit length. The applied strain in simulation is defined as $\varepsilon = (l - l_0)/l_0$, where l_0 is the lattice constant of the original structure and l is the lattice constant under the applied strain. For 2D materials, the elastic constants and moduli were obtained from Hooke's law under plane-stress conditions [31],

$$\begin{bmatrix} \sigma_{xx} \\ \sigma_{yy} \\ \sigma_{xy} \end{bmatrix} = \begin{bmatrix} C_{11} & C_{12} & 0 \\ C_{21} & C_{22} & 0 \\ 0 & 0 & C_{66} \end{bmatrix} \begin{bmatrix} \varepsilon_{xx} \\ \varepsilon_{yy} \\ 2\varepsilon_{xy} \end{bmatrix}, \quad (1)$$

where C_{11} , C_{12} , C_{21} , C_{22} , and C_{66} are the elastic stiffness constants. Young's moduli in the armchair (Y_a) and zigzag (Y_z) directions were calculated by the following formulas [32]:

$$Y_a = \frac{C_{11}C_{22} - C_{12}C_{21}}{C_{22}}, \quad (2)$$

$$Y_z = \frac{C_{11}C_{22} - C_{12}C_{21}}{C_{11}}. \quad (3)$$

Because of their trigonal crystal structures, $C_{12} = C_{21}$ and $C_{11} = C_{22}$ for α - M_2X_3 monolayers so that Y_a is equal to Y_z here. The carrier mobility can be calculated by the deformation potential theory based on the effective mass ap-

proximation, which is expressed by the following formulas for a 2D system [33]:

$$\mu_x = \frac{e\hbar^3 \left(\frac{5C_{11} + 3C_{22}}{8} \right)}{k_B T (m_x)^{3/2} (m_y)^{1/2} \left(\frac{9E_{1x}^2 + 7E_{1x}E_{1y} + 4E_{1y}^2}{20} \right)}, \quad (4)$$

$$\mu_y = \frac{e\hbar^3 \left(\frac{3C_{11} + 5C_{22}}{8} \right)}{k_B T (m_x)^{1/2} (m_y)^{3/2} \left(\frac{4E_{1x}^2 + 7E_{1x}E_{1y} + 9E_{1y}^2}{20} \right)}, \quad (5)$$

where m_x and m_y are the effective masses in two different directions and E_{1x} and E_{1y} are deformation potential constants in two different directions.

III. RESULTS AND DISCUSSION

A. Geometrical and mechanical properties

Figure 1(a) shows the fully relaxed 2D α - M_2X_3 material structure, where M represents Ga, In, and X represents S, Se. These α - M_2X_3 monolayers present a 2D trigonal lattice with M -centered octahedrons and tetrahedrons stacked in the vertical direction along the z axis. The unit cell is marked by the red diamond box consisting of two M atoms and three X atoms. The lattice constant of these four materials achieves good agreements with a previous report [20] and increases slightly along with the atomic number (see Table I).

The elastic constants and Young's moduli of the four structures are listed in Table I. Young's moduli of the four materials are much smaller than that of other known two-dimensional

TABLE I. Calculated in-plane constants a (Å), elastic constants C_{ij} ($N m^{-1}$), and Young's modulus Y ($N m^{-1}$) of α - M_2X_3 , graphene, h -BN, and MoS_2 .

Structure	Reference	a	C_{11}	C_{22}	C_{12}	C_{66}	Y_a	Y_z
α - Ga_2S_3	Our paper	3.64	98.3	98.3	41.6	29.6	80.7	80.7
α - Ga_2Se_3	Our paper	3.84	79.9	79.9	34.6	24.7	64.9	64.9
α - In_2S_3	Our paper	3.92	73.0	73.0	33.3	19.8	57.8	57.8
α - In_2Se_3	Our paper	4.10	62.9	62.9	29.4	16.7	49.2	49.2
Graphene	Refs. [7,37]	2.46	349	349	72	138	334	334
h -BN	Refs. [34,38]	2.51	289.8	289.8	63.7	113.1	275.8	275.8
MoS_2	Refs. [35,39]	3.19	128.8	127.9	28.8	50	122.3	121.5

TABLE II. Calculated PBE band-gaps E_g^{PBE} (eV) and HSE band-gaps E_g^{HSE} (eV) of α - M_2X_3 , h -BN, and MoS_2 .

Structure	Reference	Type	E_g^{PBE}	E_g^{HSE}
α - Ga_2S_3	This paper	Indirect	1.67	2.71
α - Ga_2Se_3	This paper	Indirect	0.92	1.77
α - In_2S_3	This paper	Direct	1.18	1.92
α - In_2Se_3	This paper	Direct	0.78	1.44
h -BN	Ref. [41]	Direct	4.64	5.63
MoS_2	Ref. [39]	Direct	1.58	2.01

materials, such as graphene [7], h -BN [34], and MoS_2 [35]. When applying uniaxial tensile strain along the armchair direction of the α - Ga_2S_3 monolayer, the stress increases gradually until it reaches the maximum value of 8.91 N m^{-1} at the strain of 17% as shown in Fig. 1(b). In the zigzag direction, the strain corresponding to the maximum stress of 9.50 N m^{-1} is 30% [see Fig. 1(c)]. The energy increases slowly by applying strain and no saltus is observed, which indicates that there is no structural transformation in this process. The other three materials (α - Ga_2Se_3 , α - In_2S_3 , and α - In_2Se_3) also show higher ultimate deformations (see Fig. S1–S3 of the Supplemental Material (SM)) [36] compared to the 11% of MoS_2 [15] and the 6% of CrI_3 [17], which suggests that these two-dimensional materials are very elastic and ductile.

B. Electronic properties and effects of strain

Four monolayer structures are all semiconductors, among which Ga_2S_3 and Ga_2Se_3 have indirect band gaps whereas In_2S_3 and In_2Se_3 have the direct band gaps. The band gaps calculated based on the PBE functional are listed in Table II. With the increment of atomic number, the delocalization of valence electrons leads to the gradual decrease in the band gap. Figure 2(a) shows the band structure of α - Ga_2S_3 . The conduction-band minimum (CBM) is located at the Γ point, mainly dominated by Ga- s orbitals, whereas the valence-band maximum (VBM) located between the Γ and M points is mainly composed of S- p orbitals. This is similar to the very recent results on the Janus monolayer Ga_2SX_2 ($X = \text{O}, \text{S}, \text{Se}, \text{Te}$) calculated by the QUANTUM ESPRESSO code [40]. The other three structures show similar results (see Fig. S4 of the Supplemental Material [36]) except that the VBM of α - In_2S_3

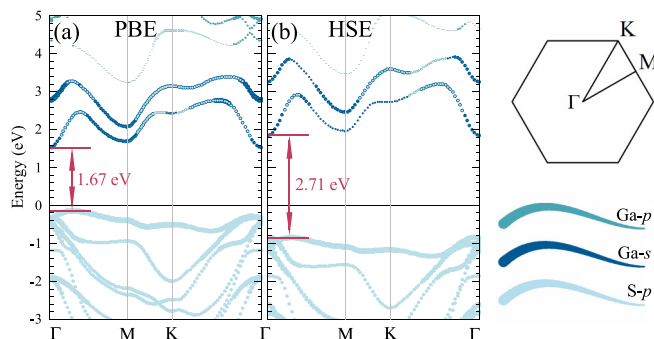


FIG. 2. Band structures of the α - Ga_2S_3 monolayer calculated based on (a) the PBE functional and (b) the HSE functional.

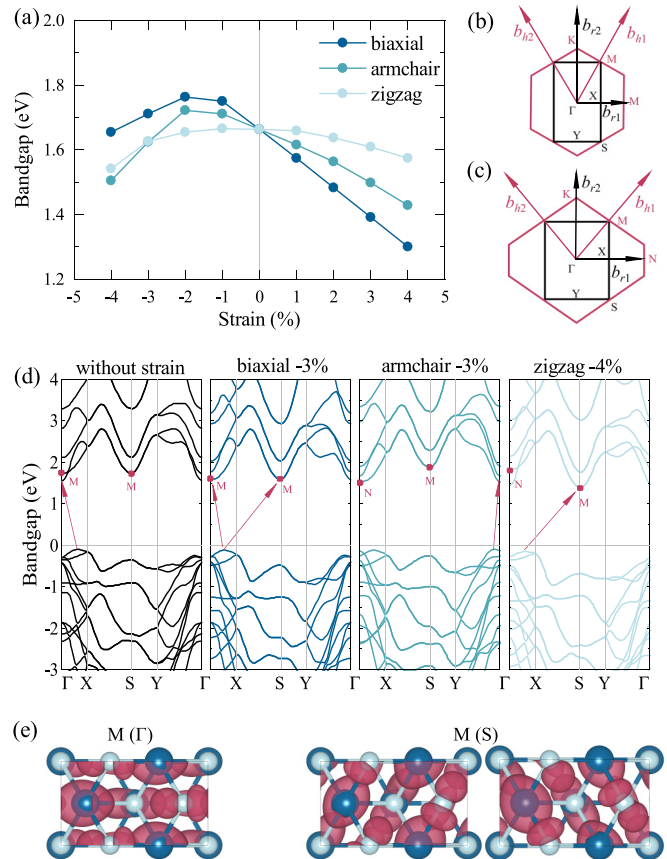


FIG. 3. (a) Band gap of the α - Ga_2S_3 monolayer under three types of strain. Schematic of Brillouin-zone folding under (b) biaxial and (c) uniaxial strain. The b_h and b_r are reciprocal lattice vectors of the hexagonal and rectangular cells, respectively. (d) The changes in band structure under several special strains. (e) The state density at M points in real space of the α - Ga_2S_3 monolayer, the value of the isosurface is $0.003 e/\text{\AA}^3$.

and α - In_2Se_3 is located at the Γ point, thus, indicating the direct band-gap property. Since the PBE functional tends to underestimate the band gap of semiconductors, we used the HSE06 functional for more accurate band structures. Table II shows that the band gaps calculated based on the HSE06 functional are significantly increased, which are similar to h -BN [41], MoS_2 [39], and previously calculated results of α - M_2X_3 monolayers [21,40]. However, as can be seen from Fig. 2(b), the band structure and the contribution of each atomic orbital at band edges are similar to those obtained by the PBE functional in Fig. 2(a) except that the value of the band gap increases from 1.67 to 2.71 eV. The band structures of the other three materials are shown in Fig. S4 of the Supplemental Material [36]. A strain-adjustable band gap of the α - Ga_2S_3 monolayer under three different types of strain is shown in Fig. 3(a). Note that a rectangular supercell is used in this section as it provides a clearer pathway to apply strain in either the armchair(x) or zigzag(y) direction as shown in Fig. 1(a). The rectangular cell is twice the size of the primitive cell, so the reciprocal lattice vector decreases, and the Brillouin zone folds as illustrated in Fig. 3(b). The band structures in Fig. 3(d) indicate the compressive strain lowers

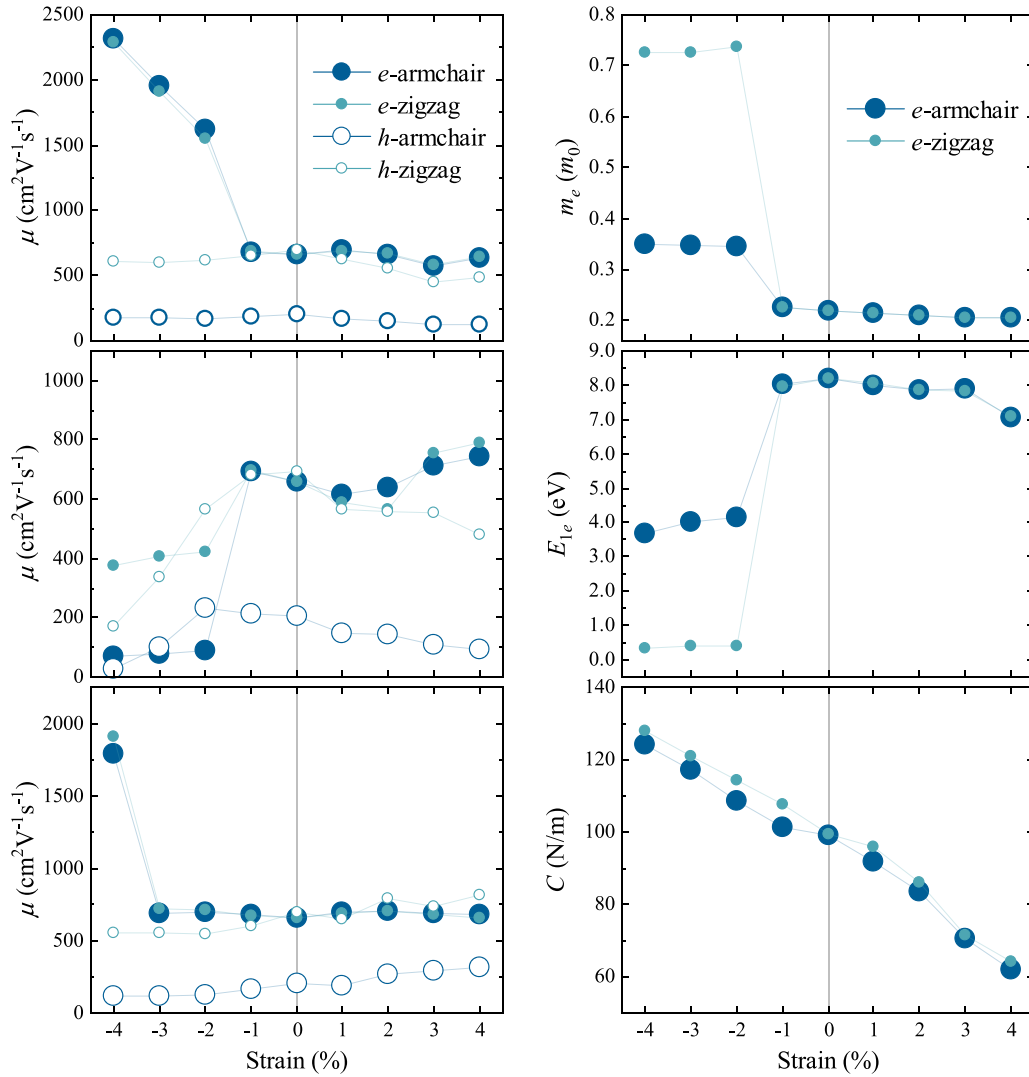


FIG. 4. (a) Carrier mobilities of the α -Ga₂S₃ monolayer under three types of strain at room temperature ($T = 300$ K). (b) Electron effective mass, electron deformation potential constant, and elastic modulus of the α -Ga₂S₃ monolayer under biaxial strain.

the band edge at $M(S)$ and $M(\Gamma)$ points. Here, the $M(S)$ and $M(\Gamma)$ points are three degenerated M points in the hexagonal Brillouin zone with two points corresponding to the S points in the rectangular case and the other one folding back to the Γ point. The state density at M points in real space indicates the sp^3 hybridizations between Ga and surrounding S atoms. The top view shows that the hybrid orbitals projected in the horizontal plane are inclined at an angle of 120° to each other [see Fig. 3(e)]. These orbitals energetically degenerate in the trigonal lattice of Ga₂S₃ without strain or with biaxial strains. However, the situation changes when applying the uniaxial strains. For example, when the strain is only applied in the x direction, the orbitals at $M(\Gamma)$ points are affected larger than those at $M(S)$ points, thus, three M points are no longer in degeneracy. This is in agreement with the deformation of the Brillouin zone under uniaxial strain as shown in Fig. 3(c). The N point folded back to the Γ point is no longer equivalent to the other $M(S)$ points due to the break in structural symmetry. In Fig. 3(d), the band structures under uniaxial strain have different CBMs located at the N point with armchair strain and at the M point with zigzag strain, which corroborates

the above physical picture and explains the different behavior of the strain-adjustable band gap in Fig. 3(a). Considering the burden of calculation and the similarity of band structure between PBE and HSE, here we only calculated the change in band gap based on the PBE functional. Note that the applied strain not only brings about the change in the band gap, but also causes the adjustment of the band edge position, thus, it would also result in tunable carrier mobility in this system.

C. Carrier mobility

Carrier mobility is an important property to measure semiconductor performance [42–44]. Therefore, we calculated the carrier mobility along with different directions of the α -Ga₂S₃ monolayer at room temperature ($T=300$ K). The electron mobilities along with the armchair and the zigzag directions are both about $657 \text{ cm}^2 \text{ V}^{-1} \text{ s}^{-1}$, whereas the hole mobilities show clear anisotropy of 204 and $694 \text{ cm}^2 \text{ V}^{-1} \text{ s}^{-1}$, respectively. Under different types of strain, the carrier mobility of the α -Ga₂S₃ monolayer changes as shown in Fig. 4(a). The hole mobilities along with the armchair and

the zigzag directions have no significant changes under biaxial strain and the anisotropy remains. However, the electron mobilities along both directions increase suddenly at -2% compressive strain and further increase as the compression intensifies. At -4% biaxial strain, the electron mobility reaches $2200\text{--}2400\text{ cm}^2\text{ V}^{-1}\text{ s}^{-1}$, which is more than three times the value without strain. According to formulas (4) and (5), the significant increase in mobility is due to the change of carrier effective mass, deformation potential, and elastic modulus. At -2% and larger biaxial compressive strains, the position of the CBM shifts to the $M(\Gamma)$ point. Although the larger curvature of the band at the $M(\Gamma)$ point corresponds to the increase in the electron effective mass, the deformation potential here drops more significantly as shown in Fig. 4(d). In addition, the elastic modulus gradually increases with compression. These factors together account for the significant increase in electron mobility. The mobility changes are opposite under the two directions of uniaxial compressive strain. For strain in the armchair direction, the electron and hole mobilities decrease slightly when the compression is greater than -2% , whereas in the zigzag direction, the electron mobility increases significantly when the compressive strain is at -4% , reaching $1700\text{--}2000\text{ cm}^2\text{ V}^{-1}\text{ s}^{-1}$, which is about three times of the value without strain. These changes can also be explained by abrupt changes in effective mass and deformation potential caused by the shift of the band edges. More details can be found in the SM [36].

D. Stability

Last but not least, it is necessary to study the stability of this series of structures, which is important for their future applications on the industrial scale. First, the formation of these structures are evaluated by the thermodynamic phase diagram which is a useful tool for evaluating the stability [45]. The other 2D compounds, MX and M_3X_4 [46–52] are included for comparison.

We calculated the formation enthalpy (ΔH) of these M_nX_m monolayers by using the following formula [53]:

$$\Delta H = \frac{E(M_nX_m) - n\mu_M - m\mu_X}{n + m}, \quad (6)$$

where $E(M_nX_m)$ is the energy of the M_nX_m monolayer, μ_M and μ_X are the chemical potential of M and X atoms in their bulk phase, n and m are the numbers of the M and X atoms, respectively. The chemical potential in the experimental environment must satisfy the following equation, thus, the M_nX_m monolayers could be grown [54]:

$$\frac{n\Delta\mu_M + m\Delta\mu_X}{n + m} > \Delta H, \quad (7)$$

here, $\Delta\mu_M$ and $\Delta\mu_X$ are the deviation value of the chemical potential from their source bulk phase. Thus, we obtained the thermodynamic competition diagram of the three 2D Ga_nS_m depending on the chemical potential as shown in Fig. 5(a). The bottom lines of three Ga_nS_m monolayers indicate the above areas are the possible region of these specific phases. Note that bulk Ga ($m = 0$) and bulk S ($n = 0$) are the reference phases and can be formed in the condition of $\Delta\mu_{Ga} > 0$ and $\Delta\mu_S > 0$. Generally, the chemical poten-

tials can be adjustable for different feedstock at different temperatures and pressures in experiments. The blue and cyan areas denote the monophase regions of Ga_2S_3 and GaS monolayers, respectively. The monophase region of the other three $\alpha\text{-}M_2X_3$ also exists in the phase diagrams as shown in Fig. S5 in the Supplemental Material [36]. The large-scale 2D $\alpha\text{-}Ga_2S_3$ nanosheet has successfully grown through the CVD method [18]. Therefore, it is expected that the other three 2D $\alpha\text{-}M_2X_3$ could realize under carefully controlled experimental conditions.

From the mechanical point of view, the elastic constants of a 2D sheet need to satisfy the stability criteria of $C_{11}C_{22} - C_{12}C_{21} > 0$ and $C_{66} > 0$ [55]. The calculated results of the $\alpha\text{-}M_2X_3$ monolayer listed in Table I meet the stability criteria, ensuring the stability of these materials in the aspect of mechanics. In addition, phonon dispersions of the four structures are calculated as shown in Fig. 5(b), and the absence of imaginary modes in the Brillouin zone verifies their kinetic stability. Note that, the frequencies in acoustic modes at the Γ point should be zero. Here, the small imaginary frequencies can be gradually improved by further expanding the supercell and with higher computational accuracy.

Relevant literature indicates that superoxide radicals near the surface are one of the main causes of oxidative degradation [56]. When the energy of the CBM is higher than the redox potential of O_2/O_2^- , excited electrons have a higher probability of transitioning to the O_2 near the surface and forming superoxide radicals. Therefore, verifying the relative position of the CBM and the redox potential is important to determine the environmental stability of materials [57,58]. As shown in Fig. 5(c), the calculated CBM positions of the four materials are all lower than the redox potential of O_2/O_2^- , which indicates that the oxidative degradation induced by superoxide radicals is unlikely to happen and, thus, brings benefits to their environmental stability.

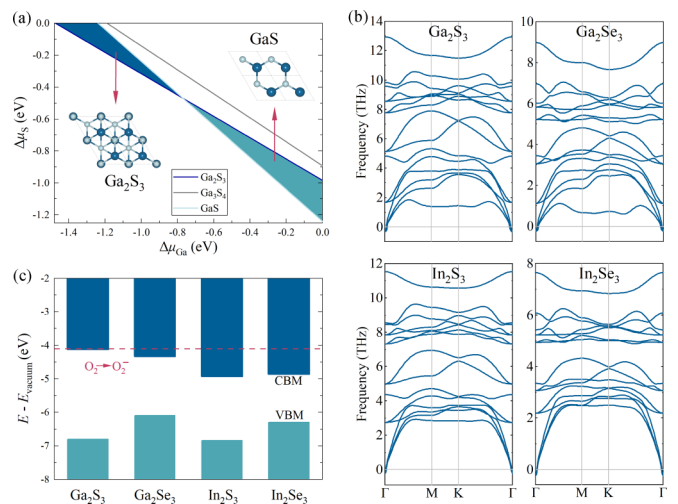


FIG. 5. (a) The thermodynamic phase diagram of Ga_nS_m monolayers. The insets are the top view of the Ga_2S_3 and GaS monolayers. (b) The phonon dispersion of the $\alpha\text{-}M_2X_3$ monolayers. (c) The energy of the VBM and CBM relative to vacuum potential of the $\alpha\text{-}M_2X_3$ monolayers where the dashed line identifies the redox potential of O_2/O_2^- .

IV. CONCLUSION

We investigated the mechanical and electronic properties of α - M_2X_3 ($M = \text{Ga, In}$; $X = \text{S, Se}$) monolayers based on first-principles calculations. These four monolayers are all semiconductors with moderate band gaps. Their Young's modulus are much lower than those of existing two-dimensional semiconductors, and the ultimate deformation reaches as high as 30%. Take the α - Ga_2S_3 monolayer as an example, the strain can effectively change the electronic band structure and greatly promote carrier mobility. We also predicted the possibility of the existence of these α - M_2X_3 monolayers by confirming the stability in terms of thermodynamic competitions, mechanics, and dynamics. In addition, their CBM is found lower than the

redox potential of O_2/O_2^- , which prevents a rapid oxidation degradation induced by superoxide radicals on the surface. This paper offers more candidates for applications of 2D materials in flexible electronic devices and nanoscale sensors.

ACKNOWLEDGMENTS

This work was supported by the Natural Science Funds of China Grant No. 21973011 and the Fundamental Research Funds for the Central Universities of China. We acknowledge the computational resources at the Big Data Computing Center of Southeast University and the National Supercomputing Center in Tianjin.

-
- [1] Z. Lin, Y. Liu, U. Halim, M. Ding, Y. Liu, Y. Wang, C. Jia, P. Chen, X. Duan, C. Wang, F. Song, M. Li, C. Wan, Y. Huang, and X. Duan, *Nature (London)* **562**, 254 (2018).
- [2] P. Cui, J. H. Choi, W. Chen, J. Zeng, C. K. Shih, Z. Li, and Z. Zhang, *Nano Lett.* **17**, 1097 (2017).
- [3] O. Kyriienko, D. N. Krizhanovskii, and I. A. Shelykh, *Phys. Rev. Lett.* **125**, 197402 (2020).
- [4] K. S. Burch, D. Mandrus, and J. G. Park, *Nature (London)* **563**, 47 (2018).
- [5] Q. Chen, R. Wang, Z. Huang, S. Yuan, H. Wang, L. Ma, and J. Wang, *Nanoscale* **13**, 6024 (2021).
- [6] Y. Wang, F. Li, Y. Li, and Z. Chen, *Nat. Commun.* **7**, 11488 (2016).
- [7] B. Wang, Q. Wu, Y. Zhang, L. Ma, and J. Wang, *ACS Appl. Mater. Interfaces* **11**, 33231 (2019).
- [8] O. A. Araromi, M. A. Graule, K. L. Dorsey, S. Castellanos, J. R. Foster, W. H. Hsu, A. E. Passy, J. J. Vlassak, J. C. Weaver, C. J. Walsh, and R. J. Wood, *Nature (London)* **587**, 219 (2020).
- [9] A. Chortos, J. Liu, and Z. Bao, *Nature Mater.* **15**, 937 (2016).
- [10] H. Lee, T. K. Choi, Y. B. Lee, H. R. Cho, R. Ghaffari, L. Wang, H. J. Choi, T. D. Chung, N. Lu, T. Hyeon, S. H. Choi, and D. H. Kim, *Nat. Nanotechnol.* **11**, 566 (2016).
- [11] Q. Cao, J. Tersoff, D. B. Farmer, Y. Zhu, and S.-J. Han, *Science* **356**, 1369 (2017).
- [12] H. Lee, S. Bak, J. Kim, and H. Lee, *Nano Res.* **14**, 198 (2021).
- [13] K. Myny, *Nat. Electron.* **1**, 30 (2018).
- [14] X. Shi, H. Chen, F. Hao, R. Liu, T. Wang, P. Qiu, U. Burkhardt, Y. Grin, and L. Chen, *Nature Mater.* **17**, 421 (2018).
- [15] S. Bertolazzi, J. Brivio, and A. Kis, *ACS Nano* **5**, 9703 (2011).
- [16] A. Falin, Q. Cai, E. J. G. Santos, D. Scullion, D. Qian, R. Zhang, Z. Yang, S. Huang, K. Watanabe, T. Taniguchi, M. R. Barnett, Y. Chen, R. S. Ruoff, and L. H. Li, *Nat. Commun.* **8**, 15815 (2017).
- [17] F. Cantos-Prieto, A. Falin, M. Alliat, D. Qian, R. Zhang, T. Tao, M. R. Barnett, E. J. G. Santos, L. H. Li, and E. Navarro-Moratalla, *Nano Lett.* **21**, 3379 (2021).
- [18] Y. Zheng, X. Tang, W. Wang, L. Jin, and G. Li, *Adv. Funct. Mater.* **31**, 2008307 (2021).
- [19] J. Lu, J. Yao, J. Yan, W. Gao, L. Huang, Z. Zheng, M. Zhang, and J. Li, *Mater. Horiz.* **7**, 1427 (2020).
- [20] W. Ding, J. Zhu, Z. Wang, Y. Gao, D. Xiao, Y. Gu, Z. Zhang, and W. Zhu, *Nat. Commun.* **8**, 14956 (2017).
- [21] L. Hu and X. Huang, *RSC Adv.* **7**, 55034 (2017).
- [22] C. Jastrzebski, D. J. Jastrzebski, V. Kozak, K. Pietak, M. Wierzbicki, and W. Gebicki, *Mater. Sci. Semicond. Process.* **94**, 80 (2019).
- [23] G. Kresse and J. Furthmüller, *Phys. Rev. B* **54**, 11169 (1996).
- [24] J. P. Perdew, K. Burke, and M. Ernzerhof, *Phys. Rev. Lett.* **77**, 3865 (1996).
- [25] P. E. Blochl, *Phys. Rev. B* **50**, 17953 (1994).
- [26] H. J. Monkhorst and J. D. Pack, *Phys. Rev. B* **13**, 5188 (1976).
- [27] J. Heyd, J. E. Peralta, G. E. Scuseria, and R. L. Martin, *J. Chem. Phys.* **123**, 174101 (2005).
- [28] T. M. Henderson, J. Paier, and G. E. Scuseria, *Phys. Status Solidi B* **248**, 767 (2011).
- [29] A. Togo, F. Oba, and I. Tanaka, *Phys. Rev. B* **78**, 134106 (2008).
- [30] J. Ihm, A. Zunger, and M. L. Cohen, *J. Phys. C: Solid State Phys.* **12**, 4409 (1979).
- [31] J. Zhou and R. Huang, *J. Mech. Phys. Solids* **56**, 1609 (2008).
- [32] J. W. Jiang and H. S. Park, *Nat. Commun.* **5**, 4727 (2014).
- [33] H. Lang, S. Zhang, and Z. Liu, *Phys. Rev. B* **94**, 235306 (2016).
- [34] R. C. Andrew, R. E. Mapasha, A. M. Ukpogon, and N. Chetty, *Phys. Rev. B* **85**, 125428 (2012).
- [35] K. Liu, Q. Yan, M. Chen, W. Fan, Y. Sun, J. Suh, D. Fu, S. Lee, J. Zhou, S. Tongay, J. Ji, J. B. Neaton, and J. Wu, *Nano Lett.* **14**, 5097 (2014).
- [36] See Supplemental Material at <http://link.aps.org/supplemental/10.1103/PhysRevB.105.235303> for stress-strain curves and band structures of the α - Ga_2Se_3 , α - In_2S_3 , and α - In_2Se_3 monolayers; carrier mobility and other relevant parameters of the α - Ga_2S_3 monolayer under different types of strain.
- [37] J. M. Carlsson and M. Scheffler, *Phys. Rev. Lett.* **96**, 046806 (2006).
- [38] M. Topsakal, E. Aktürk, and S. Ciraci, *Phys. Rev. B* **79**, 115442 (2009).
- [39] K. Kośmider and J. Fernández-Rossier, *Phys. Rev. B* **87**, 075451 (2013).
- [40] N. N. Hieu, H. V. Phuc, A. I. Kartamyshev, and T. V. Vu, *Phys. Rev. B* **105**, 075402 (2022).

- [41] B. Chettri, P. K. Patra, N. N. Hieu, and D. P. Rai, *Surf. Interfaces* **24**, 101043 (2021).
- [42] M. Long, L. Tang, D. Wang, Y. Li, and Z. Shuai, *ACS Nano* **5**, 2593 (2011).
- [43] Y. Wang, X. Tang, Q. Zhou, X. Chen, Q. Chen, and Y. Xu, *Phys. Rev. B* **102**, 165428 (2020).
- [44] L. Cheng, C. Zhang, and Y. Liu, *J. Am. Chem. Soc.* **141**, 16296 (2019).
- [45] M. Ider, R. Pankajavalli, W. Zhuang, J. Y. Shen, and T. J. Anderson, *ECS J. Solid State Sci. Technol.* **4**, Q51 (2015).
- [46] D. J. Late, B. Liu, H. S. S. R. Matte, C. N. R. Rao, and V. P. Dravid, *Adv. Funct. Mater.* **22**, 1894 (2012).
- [47] G. Han, Z.-G. Chen, L. Yang, L. Cheng, J. Drennan, and J. Zou, *Cryst. Growth Des.* **13**, 5092 (2013).
- [48] V. Zólyomi, N. D. Drummond, and V. I. Fal'ko, *Phys. Rev. B* **87**, 195403 (2013).
- [49] L. Debbichi, O. Eriksson, and S. Lebègue, *Ann. Phys. (Berlin)* **526**, 402 (2014).
- [50] G. Han, Z.-G. Chen, C. Sun, L. Yang, L. Cheng, Z. Li, W. Lu, Z. M. Gibbs, G. J. Snyder, K. Jack, J. Drennan, and J. Zou, *CrystEngComm* **16**, 393 (2014).
- [51] M. Yagmurcukardes, R. T. Senger, F. M. Peeters, and H. Sahin, *Phys. Rev. B* **94**, 245407 (2016).
- [52] S. Demirci, N. Avazlı, E. Durgun, and S. Cahangirov, *Phys. Rev. B* **95**, 115409 (2017).
- [53] M. J. Mehl, D. Finkenstadt, C. Dane, G. L. W. Hart, and S. Curtarolo, *Phys. Rev. B* **91**, 184110 (2015).
- [54] S.-H. Wei, *Comput. Mater. Sci.* **30**, 337 (2004).
- [55] J. H. Kim, J. H. Jeong, N. Kim, R. Joshi, and G.-H. Lee, *J. Phys. D: Appl. Phys.* **52**, 083001 (2019).
- [56] A. Favron, E. Gaufres, F. Fossard, A. L. Phaneuf-L'Heureux, N. Y. Tang, P. L. Levesque, A. Loiseau, R. Leonelli, S. Francoeur, and R. Martel, *Nature Mater.* **14**, 826 (2015).
- [57] Y. Wang, C. Jiang, Q. Chen, Q. Zhou, H. Wang, J. Wan, L. Ma, and J. Wang, *J. Phys. Chem. Lett.* **9**, 6847 (2018).
- [58] X. Niu, Y. Li, Y. Zhang, Q. Li, Q. Zhou, J. Zhao, and J. Wang, *J. Phys. Chem. Lett.* **9**, 5034 (2018).